

# Cation-Induced Interfacial Hydrophobic Microenvironment Promotes the C–C Coupling in Electrochemical CO<sub>2</sub> Reduction

Xinzhe Yang, Haowen Ding, Shunning Li, Shisheng Zheng,\* Jian-Feng Li, and Feng Pan\*



Cite This: *J. Am. Chem. Soc.* 2024, 146, 5532–5542



Read Online

ACCESS |



Metrics & More

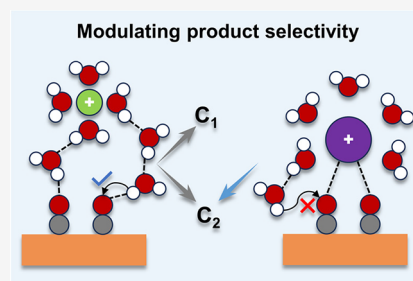


Article Recommendations



Supporting Information

**ABSTRACT:** The electrochemical carbon dioxide reduction reaction (CO<sub>2</sub>RR) toward C<sub>2</sub> products is a promising way for the clean energy economy. Modulating the structure of the electric double layer (EDL), especially the interfacial water and cation type, is a useful strategy to promote C–C coupling, but atomic understanding lags far behind the experimental observations. Herein, we investigate the combined effect of interfacial water and alkali metal cations on the C–C coupling at the Cu(100) electrode/electrolyte interface using ab initio molecular dynamics (AIMD) simulations with a constrained MD and slow-growth approach. We observe a linear correlation between the water-adsorbate stabilization effect, which manifests as hydrogen bonds, and the corresponding alleviation in the C–C coupling free energy. The role of a larger cation, compared to a smaller cation (e.g., K<sup>+</sup> vs Li<sup>+</sup>), lies in its ability to approach the interface through desolvation and coordinates with the \*CO+\*CO moiety, partially substituting the hydrogen-bonding stabilizing effect of interfacial water. Although this only results in a marginal reduction of the energy barrier for C–C coupling, it creates a local hydrophobic environment with a scarcity of hydrogen bonds owing to its great ionic radius, impeding the hydrogen of surrounding interfacial water to approach the oxygen of the adsorbed \*CO. This skillfully circumvents the further hydrogenation of \*CO toward the C<sub>1</sub> pathway, serving as the predominant factor through which a larger cation facilitates C–C coupling. This study unveils a comprehensive atomic mechanism of the cation–water–adsorbate interactions that can facilitate the further optimization of the electrolyte and EDL for efficient C–C coupling in CO<sub>2</sub>RR.



## INTRODUCTION

The electrochemical carbon dioxide reduction reaction (CO<sub>2</sub>RR) into fuels and chemicals is a promising approach to close the carbon cycle and to store electricity generated by renewable energy.<sup>1</sup> Among the various reduction products, C<sub>2</sub> products have attracted substantial attention due to their high economic value that can act as the building blocks for long-chain hydrocarbons, oxygenates, and polymers.<sup>2</sup> Copper (Cu) is the only transition metal capable of the electrochemical reduction of CO<sub>2</sub> to multicarbon products.<sup>3,4</sup> However, it faces the bottleneck of product selectivity with concurrent formation of HCOOH, CO, CH<sub>4</sub>, C<sub>2</sub>H<sub>4</sub>, CH<sub>3</sub>CH<sub>2</sub>OH, etc., hindering its industrial application.<sup>5</sup>

To improve the efficiency of C–C coupling toward C<sub>2</sub> products on copper, enormous efforts have been devoted to the chemical modification of catalysts by doping, alloying, and morphology optimization.<sup>6–11</sup> Essentially, these strategies aim to regulate the solid side of the solid–electrolyte interface, also known as the electric double layer (EDL). In recent years, the management of the solution side has received increasing attention due to its ease of manipulation and its universal application across different electrode materials.<sup>12–18</sup>

Under the ambient conditions of the CO<sub>2</sub>RR, the main solution components present at the electrode interface are interfacial water molecules and cations. H<sub>2</sub>O is the most practical solvent molecule. Understanding the structure and

dynamic process of H<sub>2</sub>O at the EDL is an extremely significant topic in electrochemistry.<sup>19–24</sup> The interfacial water molecules play diverse roles in CO<sub>2</sub> electroreduction. On the one hand, they exhibit a significant stabilizing effect on intermediate species in the CO<sub>2</sub>RR, which could benefit the C<sub>2</sub> selectivity.<sup>25–28</sup> However, on the other hand, they serve as the proton donors for the hydrogenation steps, thereby possibly facilitating the deep reduction of CO<sub>2</sub> toward C<sub>1</sub> products and undergoing the side reaction of hydrogen evolution reaction (HER), impeding the generation of C<sub>2</sub> products.<sup>29–31</sup> Reducing the activity of water molecules can effectively suppress the HER, enhancing the selectivity of C<sub>2</sub> products.<sup>32</sup>

As for cations, the Faradaic efficiency of C<sub>2</sub> products from CO<sub>2</sub> or also CO as reactants exhibits a surprising size dependence,<sup>33–35</sup> following the order Li<sup>+</sup> < Na<sup>+</sup> < K<sup>+</sup> < Rb<sup>+</sup> < Cs<sup>+</sup>. Bell and co-workers demonstrated that larger cations can be better enriched at the outer Helmholtz plane and stabilize

Received: December 3, 2023

Revised: January 9, 2024

Accepted: January 31, 2024

Published: February 16, 2024



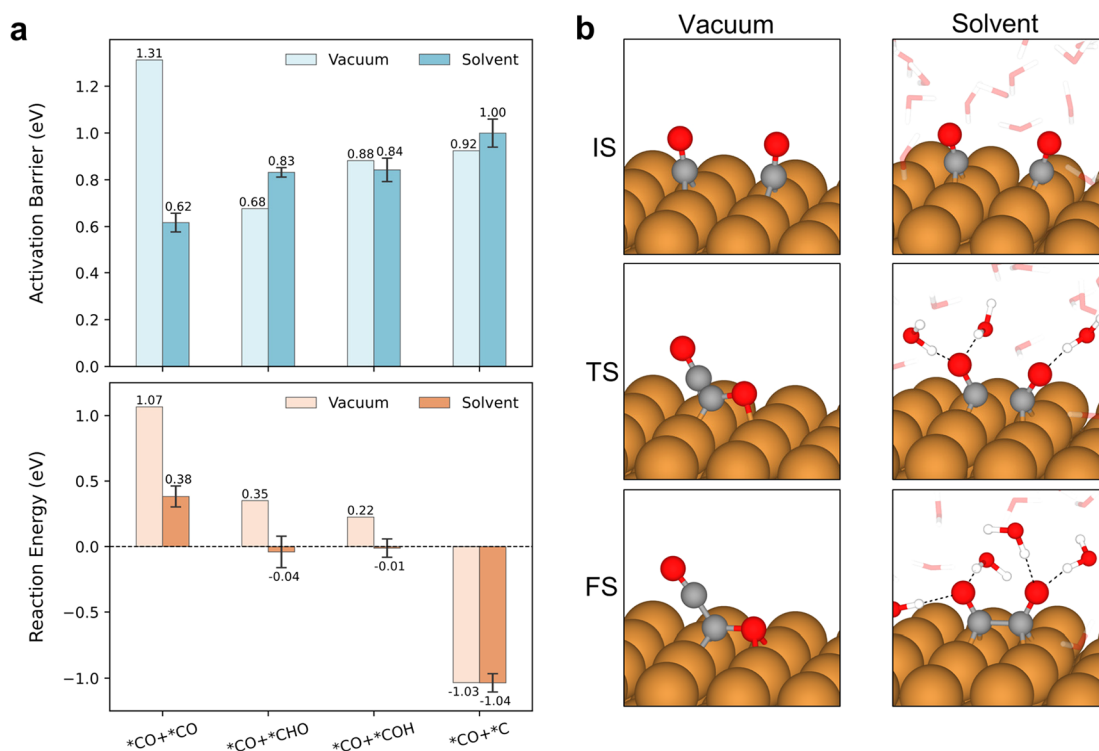


**Figure 1.** C–C coupling in the vacuum and solvent environment. (a) Free energy profiles for \*CO+\*CO, \*CO+\*CHO, \*CO+\*COH, and \*CO+\*C coupling reactions. Error bars (standard deviation) were calculated for the solvent environment based on five independent simulations. (b) Representative structures depicting the initial, transition, and final states during the CO dimerization reaction. Color code: Cu, brown; O, red; H, white; C, gray.

intermediates through electrostatic dipole interactions.<sup>33</sup> Chan et al. suggested that the cations can affect CO<sub>2</sub>RR by adjusting the interfacial electric field.<sup>36</sup> Large cations (e.g., K<sup>+</sup>) often have small hydrated radius and tend to be partially desolvated.<sup>37</sup> Yang and co-workers highlighted that the direct coordination interaction between the intermediates with cations is key to stabilize the \*CO dimer. However, the calculated difference in the kinetic barrier for C–C coupling with different cations is minor within 0.1 eV.<sup>38</sup> Rossmeisl et al. demonstrated that the different alkali metal cations negligibly change the thermodynamics for C<sub>2</sub> products while may affect the kinetics of the protonation step.<sup>39</sup> Notably, the presence of cations may alter the configuration of the interfacial water molecules and the distribution of the hydrogen bond network<sup>21,40</sup> and thus exert influence on the CO<sub>2</sub> reduction. Cheng's group suggested that the cation with a higher Helmholtz capacitance can result in higher negative surface charge density under the same electrode potential, which further manifests in the different number of hydrogen bonds on the adsorbed \*CO to lower the activation of C–C coupling.<sup>41</sup> Despite these advances, the influence of interfacial water and cations on C–C coupling remains elusive and controversial, in particular, the distinct roles of interfacial waters and cations in C–C coupling and their potential interchangeability, given they both have the ability to stabilize intermediates, as demonstrated by previous works.<sup>28,38</sup> Recent studies indicated that the cation coordination is essential for the CO<sub>2</sub> activation, while there is no reduction activity without metal cations,<sup>42,43</sup> but does this hold for C–C coupling? The understanding of how cations regulate the diverse roles of interfacial water and the impact of such regulations on C–C coupling is also lacking.

In this work, we theoretically investigate the combined effect of interfacial water and alkali metal cations on the C–C coupling at the Cu(100) electrode/electrolyte interface using ab initio molecular dynamics (AIMD) simulations with a constrained MD and slow-growth approach. We identified the stabilizing effects of interfacial water on various C–C coupling reaction modes, demonstrating a linear correlation between water–adsorbate interactions, which manifests as hydrogen bonds, and the associated alleviation in the coupling barrier. Water molecules exhibit the most pronounced stabilizing effect in the CO dimerization mode for C–C coupling due to the strong electron localization effect on the oxygen of \*CO+\*CO intermediates. The energetic impact of different cations on the \*CO dimerization is subtle. A larger cation (e.g., K<sup>+</sup> vs Li<sup>+</sup>) can desolvate and approach the interface, coordinating with \*CO+\*CO species and thus partially substituting the role of hydrogen bonds. Concurrently, it creates a local hydrophobic environment with the absence of hydrogen bonds for \*CO+\*CO owing to the large ionic radius, thereby mitigating the adverse effects of interfacial water molecules, that is, preventing the hydrogen atoms of surrounding water from attacking the oxygen atoms of adsorbed \*CO, which helps disrupt the further hydrogenation toward C<sub>1</sub> products and consequently boosting the efficiency of C–C coupling toward the C<sub>2</sub> pathway. Collectively, we demonstrate a complete atomic mechanism of the cation–water–adsorbate interactions for steering the C–C coupling in the electrochemical CO<sub>2</sub>RR on copper.

## COMPUTATIONAL DETAILS

The Cu(100) surface represents a primary facet of polycrystalline copper<sup>44</sup> and is acknowledged for its elevated selectivity

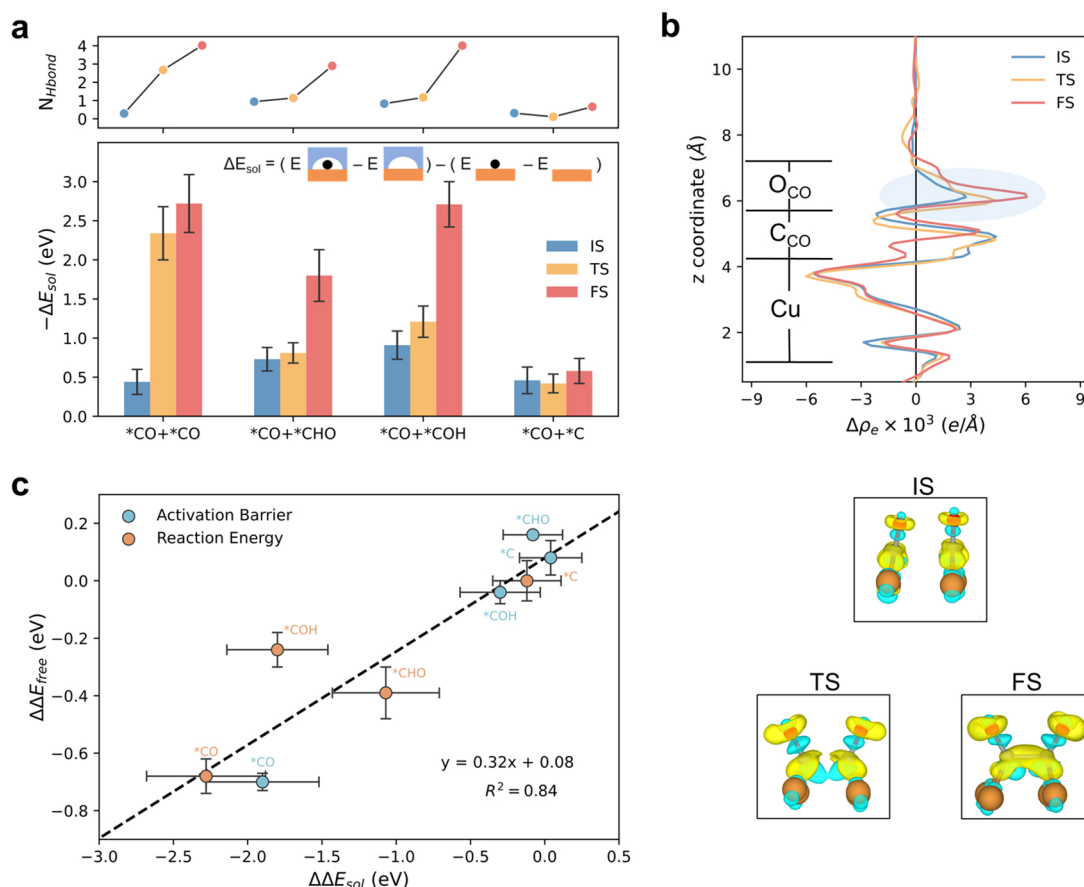


**Figure 2.** Solvation effect in C–C coupling reactions. (a) Changes in the number of hydrogen bonds associated with the adsorbate and solvent–adsorbate interaction energies during the reaction. (b) Planar-averaged differential charge density and differential charge density isosurface contours for initial, transition, and final states during the CO dimerization reaction.  $\Delta \rho_e = \rho_{\text{Cu+ads+wat}} - \rho_{\text{Cu+wat}} - \rho_{\text{ads}}$ . Yellow and cyan denote electron accumulation and depletion, respectively (isovalue =  $0.0075 \text{ e \AA}^{-3}$ ). (c) The linear relationship between changes in solvent–adsorbate interaction energies compared to the initial state ( $\Delta \Delta E_{\text{sol}}$ ) and free energy difference between the vacuum and solvent environment ( $\Delta \Delta E_{\text{free}}$ ).

toward  $\text{C}_2$  products.<sup>45</sup> In this article, atomic-scale simulations were conducted on a three-layer  $3 \times 4$  Cu(100) slab with the bottom layer fixed in bulk positions. A vacuum region of 30 Å thickness separates the surface from its periodic image in the  $z$ -direction. The Cu(100) electrode–electrolyte interface was modeled by adding 32 explicit water molecules above the slab, resulting in an approximate water film thickness of 15 Å. A full-size visualization of this model is shown in Figure S1. Ions are introduced into the system through the substitution of a corresponding number of  $\text{H}_2\text{O}$  molecules.

All DFT-based calculations were performed using the Vienna ab initio Simulation Package (VASP)<sup>46,47</sup> employing the projector-augmented-wave (PAW) method.<sup>48</sup> The Perdew–Burke–Ernzerhof (PBE) functional within the generalized gradient approximation (GGA) framework<sup>49</sup> was utilized to describe electron exchange–correlation interactions. The D3 dispersion correction of Grimme<sup>50</sup> was added to consider the van der Waals interaction. Transition states in the vacuum model were located by combining the climbing image nudged elastic band (CI-NEB)<sup>51</sup> and dimer methods.<sup>52</sup> We performed AIMD simulations to investigate the dynamic nature of liquid water. The slow-growth approach<sup>53,54</sup> implemented in VASP was utilized to obtain the free energy profile in the solvent model. The structures of transition and final states were extracted from the slow-growth trajectories and confirmed by conducting an additional 5 ps AIMD simulation (constrained

MD is applied for the transition state). Further details of our calculations can be found in the Supporting Information.

## RESULTS AND DISCUSSION

Interfacial water molecules can interact with adsorbates through hydrogen bonds, electrostatic interactions, and possibly even chemical binding, with different adsorbates displaying distinct types of interactions.<sup>15,27,55–57</sup> Understanding these interactions and how they evolve over the course of a catalytic reaction is an important step in quantifying the energy landscape and reaction rates. Thus, we started with the investigation of the role of interfacial water molecules in the stabilization of C–C coupling. Prior research suggested various C–C coupling modes on copper surfaces.<sup>4</sup> We choose the four most plausible patterns, including \*CO–\*CO,<sup>58–61</sup> \*CO–\*CHO,<sup>62</sup> \*CO–\*COH,<sup>63</sup> and \*CO–\*C<sup>64,65</sup> to study the water–adsorbate interactions. The activation energy and reaction energy of different coupling modes in vacuum and pure water solution environments are presented in Figure 1a. Interestingly, water molecules do not always show a strong stabilizing effect. For \*CO+\*CHO and \*CO+\*C coupling modes, the solvent environment slightly elevates their activation energy. The CO dimerization is significantly regulated by the arrangements of surrounding water molecules, with the activation energy decreasing from 1.31 eV to 0.62 eV and the reaction energy decreasing from 1.07 eV to 0.38 eV.

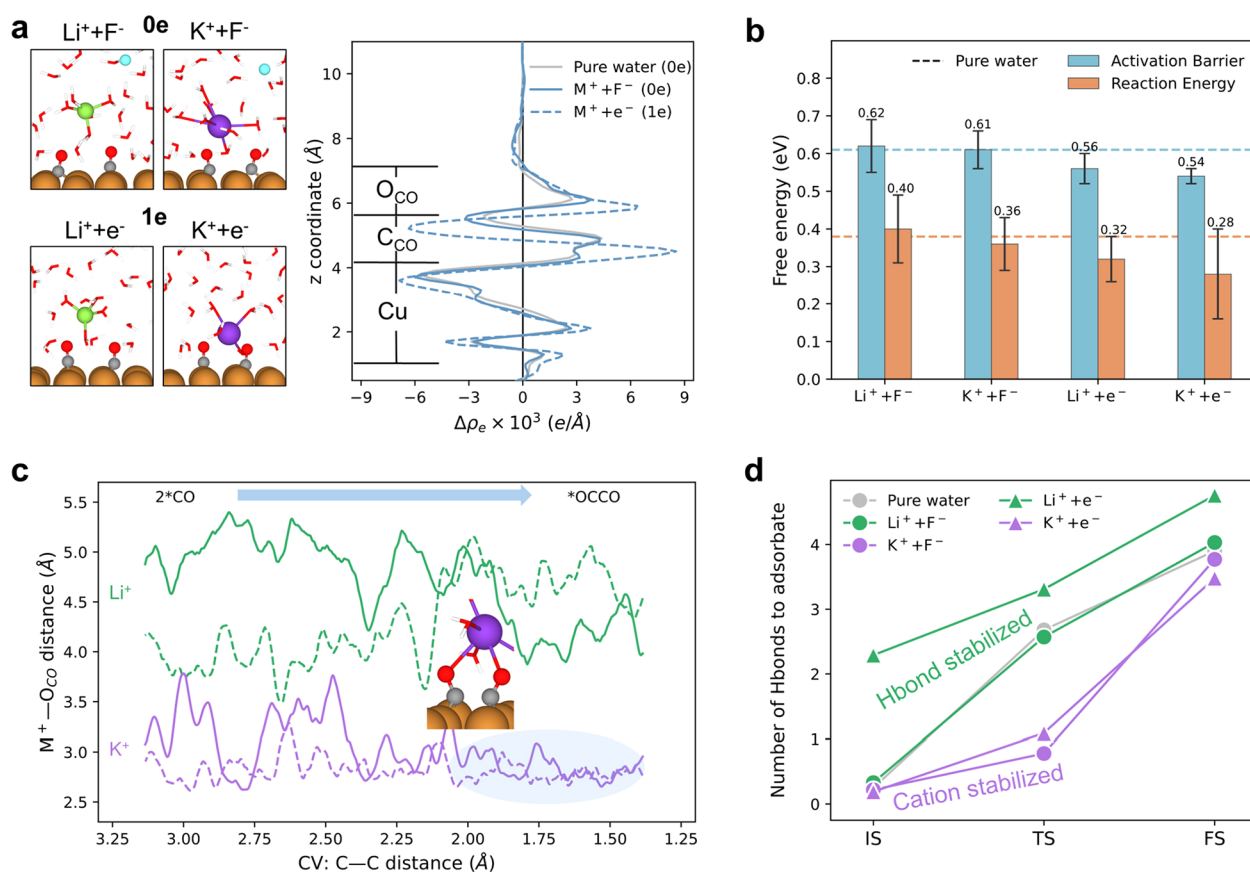


**Figure 3.** Influences of cations on the CO dimerization step. (a) Snapshots of  $M^+F^-$  and  $M^+e^-$  ( $M = \text{Li}/\text{K}$ ) models and their planar-averaged differential charge density.  $\Delta\rho_e = \rho_{\text{Cu+ads+wat+ion}} - \rho_{\text{Cu+wat+ion}} - \rho_{\text{ads}}$ . For clarity,  $\text{Li}^+F^-$  and  $\text{Li}^+e^-$  models are presented, while  $\text{K}^+F^-$  and  $\text{K}^+e^-$  models exhibit similarity to  $\text{Li}^+F^-$  and  $\text{Li}^+e^-$  (Figure S14). To clearly show the local structure of cations and adsorbates, we extracted only a portion of the entire model (Figure S1). (b) Free energy profiles of the CO dimerization under different conditions. (c) Distance of  $M^+-\text{O}_{\text{CO}}$  along the collective variable. For clarity,  $\text{Li}^+e^-$  and  $\text{K}^+e^-$  models serve as illustrative examples, with  $\text{Li}^+F^-$  and  $\text{K}^+F^-$  models having similar behavior (Figure S15). The solid line and dashed line, respectively, represent the distances between the cation and each of the two  $^*\text{CO}$  molecules. (d) Variations in the number of hydrogen bonds during CO dimerization. Color code: Cu, brown; O, red; H, white; C, gray; Li, green; K, purple; F, cyan.

Figure 1b illustrates the snapshots of the initial, transition, and final states of CO dimerization in both vacuum and solvent environments (other coupling modes are presented in Figures S4–S6). Evident configurational disparity is observed in the CO dimer, which does not appear in other reaction modes. In the vacuum environment,  $^*\text{OCCO}$  adopts a hook-like shape, with one CO parallel to the interface and the other CO oriented diagonally toward the vacuum. In the solvent environment, abundant hydrogen bonds form between surrounding water molecules and the O in  $^*\text{OCCO}$ , leading to a notable transformation of the  $^*\text{OCCO}$  configuration into two CO units both tilted toward the solvent. This result is consistent with previous works that computed the CO dimerization in the vacuum or solvent environment.<sup>6,59,61,66–68</sup>

The rearrangement of the  $^*\text{OCCO}$  configuration suggests that hydrogen bonds may be the primary contributor to solvation effects. Therefore, we conduct a statistical analysis of the number of hydrogen bonds in the initial, transition, and final states for the four different coupling modes in the solvent environment following the criterion in previous literature<sup>27</sup> (upper panel of Figure 2a). At the initial state, the  $^*\text{CO}+^*\text{CO}$  exhibits minimal hydrogen bonds ( $N_{\text{Hbond}} = 0.29$ ) due to the hydrophobic nature of CO. During the evolution to the final state, the merging of the electron clouds of the two  $^*\text{CO}$  units

results in electron transfer from C to O (Figure 2b, other coupling modes are shown in Figures S7–S9). The accumulation of charges on O gives rise to an anionic character, exerting strong electrostatic attraction to hydrogens in the surrounding water, thus forming abundant hydrogen bonds with  $N_{\text{Hbond}} = 2.68$  in the transition state and  $N_{\text{Hbond}} = 4.02$  in the final state. In other coupling modes, the variation in hydrogen bonds is relatively gradual between different states (top panel of Figure 2a). For  $^*\text{CHO}$  and  $^*\text{COH}$ , hydrogen bonds only increase during the course from the transition state to the final state, and thus the kinetic barrier may not be effectively tuned, while  $^*\text{C}$  lacks the ability to form hydrogen bonds in the whole coupling process. The solvent–adsorbate interaction energies ( $\Delta E_{\text{sol}}$ ) are calculated to quantify the hydrogen-bonding-induced stabilization effect (the calculation details are presented in the Supporting Information).<sup>55</sup> The results from the lower panel of Figure 2a demonstrate that the  $\Delta E_{\text{sol}}$  of  $^*\text{OCCO}$  indeed increases dramatically during the coupling process compared to other coupling modes. The variation in the number of hydrogen bonds physically correlates with the changes in  $\Delta E_{\text{sol}}$ . Thus, a great majority of the water–adsorbate interaction comes from those  $\text{H}_2\text{O}$  molecules that are hydrogen-bonded to the adsorbate. A larger change in  $\Delta E_{\text{sol}}$  compared to the initial state may be

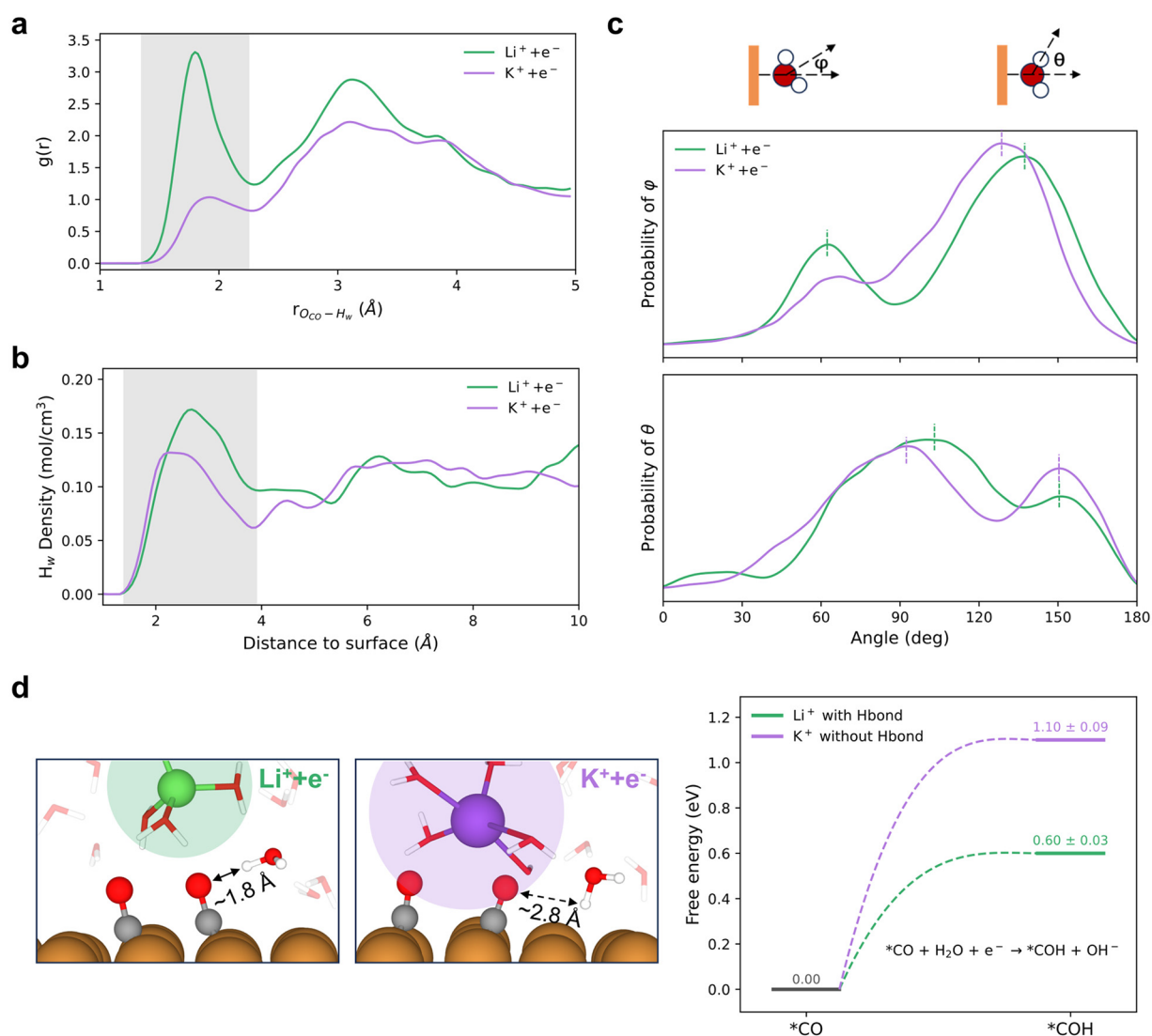


**Figure 4.** Statistical analysis of interfacial water and the protonation of  $^*\text{CO}$  in  $\text{Li}^+ + \text{e}^-$  and  $\text{K}^+ + \text{e}^-$  models. (a) Radial distribution functions (RDFs) between the O atoms of  $^*\text{CO}$  and the H atoms of water. (b) Profiles illustrating the concentration distribution of H atoms in water along the  $z$ -direction. (c) Probability distributions of the angle between the surface normal and the bisector of the water ( $\phi$ ) and the angle between the surface normal and the direction of the O–H bond direction ( $\theta$ ). The interfacial water is defined as being within a 4 Å distance from the metal surface. (d) Typical configurations representing the initial state and the free energy diagram of  $^*\text{CO}$  protonation. To clearly show the local structure of cations and adsorbates, we only extracted a portion of the entire model.

responsible for a more significant reduction in the free energy required for C–C coupling in a solvent environment compared to a vacuum environment ( $\Delta\Delta E_{\text{free}}$ ). This is confirmed by the results shown in Figure 2c, where  $\Delta\Delta E_{\text{sol}}$  and  $\Delta\Delta E_{\text{free}}$  exhibit a linear relationship for both the activation energy and the reaction energy. To the best of our knowledge, we have, for the first time, quantified the relationship between water–adsorbate interactions and the coupling energy between two carbon species, which can be generalized to analyze the evolution trends on other coupling modes, such as electrochemical  $\text{C}_1$ – $\text{C}_2$  coupling toward the  $\text{C}_3$  product<sup>9,69,70</sup> and C–N coupling toward N-containing products.<sup>71–73</sup>

Given that the  $^*\text{CO} + ^*\text{CO}$  is the most energetically favorable C–C coupling mode, which is in accordance with previous works,<sup>26,66</sup> we investigate the influence of different cations on its energetics to explore the cation-dependent  $\text{C}_2$  products selectivity observed in experiments. Four models consisting of  $\text{M}^+ + \text{F}^-$  and  $\text{M}^+ + \text{e}^-$  ( $\text{M} = \text{Li}/\text{K}$ ) are constructed

(Figure 3a). In the ion pair models of  $\text{M}^+ + \text{F}^-$ , no net charge is introduced into the system, allowing for a direct comparison with the conditions of the pure water model. Thus, they are employed to investigate the potential interchangeability of cations and interfacial water molecules on the course of CO dimerization. Differential charge density is used to examine the net charge hypothesis. The results indicate that the introduction of ion pairs (both  $\text{Li}^+ + \text{F}^-$  and  $\text{K}^+ + \text{F}^-$ ) has negligible impacts on the charge distribution of the  $^*\text{CO} + ^*\text{CO}$  configuration (Figure 3a). It is intriguing that, whether it is  $\text{Li}^+ + \text{F}^-$  or  $\text{K}^+ + \text{F}^-$ , the activation energy and reaction energy for C–C coupling are nearly identical with that of the pure water conditions (Figure 3b). However,  $\text{Li}^+$  and  $\text{K}^+$  exhibit different spatial characteristics and solvation shell evolution at the interface (Figure 3c, Figure S10, and Figure S11). The  $\text{Li}^+$  consistently stays away from the  $^*\text{CO} + ^*\text{CO}$  species with complete first and second hydration shells (Figure S11); therefore slight effects on the C–C coupling energetics can be

expected since its interface is qualitatively similar to that of the pure water environment. In contrast, the partly desolvated  $K^+$ , evidenced by the radial distribution functions (RDFs) and the evolution of the cation–surface distance (Figure S10 and Figure S11), can steadily coordinate with the O in the  $*OCCO$  moiety along the C–C coupling process with the distance of  $M^+–OCO$  less than 3.5 Å (Figure 3c). The difference in desolvation behavior of cations is qualitatively consistent with previous results and mainly depends by the nature of the cation solvation shell size (Figure S12).<sup>74,75</sup> The coordination of intermediates with the  $K^+$  cation markedly reduces the number of hydrogen bonds required for the transition state of C–C coupling (Figure 3d), indicating that  $K^+$  coordination can partially replace the role of hydrogen bonds. This also suggests that cation coordination only marginally impacts the energetics of C–C coupling, and the stabilizing effects of  $K^+$  and water molecules can be mutually substituted, which differs from the  $CO_2$  activation process. By introducing metal cations, researchers found the energy barrier is significantly reduced.<sup>43</sup> Without the cation coordination, no products of CO were experimentally observed.<sup>42</sup>

Subsequently, we examined the scenarios involving the simultaneous introduction of cations and electrons, namely, the  $Li^+e^-$  and  $K^+e^-$  models. Lithium and potassium will undergo automatic ionization, and the equal number of electrons to that of  $Li^+/K^+$  will go into the Fermi level of the metal surface, adjusting the electrode potential. They can mimic an ambient electrochemical condition, where the enrichment of cations at the interface is accompanied by a change in electrode potential.<sup>19,40</sup> The electrode potentials (Table S1) of  $Li^+e^-$  and  $K^+e^-$  models are both around  $-0.6$  V vs RHE (pH = 7), roughly corresponding to the potential that has a maximum yield of  $C_2$  products at Cu(100).<sup>34,76</sup> Thus, the following discussions are based on these charged models. Based on the analysis of differential charge density, the  $Li^+e^-$  and  $K^+e^-$  models both induce a pronounced and almost nearly uniform charging effect on the  $*CO+*CO$  configuration (Figure 3a). The additional electrons would occupy the  $2\pi^*$  orbital of  $*CO$  and thus induce an anionic character of  $*CO$ . Because the CO dimer also tends to be an anionic form as mentioned above, increasing the electron density on  $*CO+*CO$  will modulate the energy landscape of the C–C coupling process. The energy calculation results (Figure 3b) indicate that, for both  $Li^+e^-$  and  $K^+e^-$ , the activation energies of the C–C coupling reaction exhibit an evident decrease, with average values of 0.56 and 0.54 eV, respectively. However, the difference between them is still minor, suggesting that the reduction in the energy barrier is primarily attributed to the charging and activation of  $*CO$  induced by the electrode potential, and the response to electrode potential is consistent between  $Li^+$  and  $K^+$ . Taking the standard deviation caused by the fluctuation of the molecule dynamics into consideration (Figure 3b), the difference in the free energy for C–C coupling under the  $Li^+$  and  $K^+$  environments will be even more difficult to distinguish.

The above results indicate that considering only the influence of cations on the energetics of C–C coupling may be insufficient to account for the observed variations in the selectivity of  $C_2$  products among different cations in the experimental observations ( $K^+ > Li^+$ ).<sup>33</sup> It should be noted that the yield of  $C_2$  products is also significantly influenced by competition from the  $C_1$  pathway and HER. Both of these are closely related to the configuration and distribution of

interfacial water molecules. The adsorbed  $*CO$  can obtain protons from  $H_2O$  to generate  $*COH$ , which is considered as the rate-determining step for the formation of  $C_1$  products on Cu(100).<sup>77–80</sup> The hydrogenation step can be accelerated by the shortening proton transfer distance between the adsorbate and water.<sup>81–83</sup> Thus, it can be anticipated that if the oxygen in  $*CO$  forms hydrogen bonds with the interfacial water, the protonation of  $*CO$  will be energetically favorable. In the pure water environment,  $*CO$ , as a hydrophobic molecule, has negligible interactions with interfacial water molecules. In the condition of  $Li^+e^-$ , both the hydrogen-bonding count statistics and the radial distribution function of hydrogen around the oxygen of  $*CO+*CO$  (Figure 3d and Figure 4a) suggest that a significant number of protons are distributed in the first solvation shell of  $*CO$ , forming two hydrogen bonds on average. This can be attributed to the anionic character of oxygen in charged  $*CO$  (Figure 3a), exerting a stronger electrostatic attraction to the surrounding protons. Contrarily, in the  $K^+e^-$  model, the partly desolvated  $K^+$  will approach the interface closely and coordinate with  $*CO+*CO$  ( $\sim 3–3.5$  Å), which does not occur in the  $Li^+e^-$  model ( $\sim 4–5$  Å, Figure 3c) and is similar to that of the ion pair model. The larger radius of the potassium ion employs significant repulsion on the surrounding water, reducing the probability of protons appearing around  $*CO$  and thus the absence of hydrogen bonds according to the hydrogen-bonding count statistics, the radial distribution function, and also the hydrogen density distribution along the  $z$  direction (Figure 3d, Figure 4a, and Figure 4b).

The configuration of interfacial water, which is quantified by the angle between the surface normal and the bisector of the water ( $\varphi$ ) and the angle between the surface normal and the O–H bond direction ( $\theta$ ), is further statistically analyzed to illustrate the different influences of  $Li^+$  and  $K^+$  on the protonation of  $*CO$  (Figure 4c). In the  $Li^+e^-$  environment, two obvious peaks at  $\sim 60^\circ$  and  $\sim 140^\circ$  in the  $\varphi$  distribution and two main peaks at  $\sim 100^\circ$  and  $\sim 150^\circ$  in the  $\theta$  distribution are observed. This indicates that there are two types of interfacial water molecules in the  $Li^+e^-$  model. The first type adsorbs at the interface, with its two hydrogens slightly oriented toward the bulk solution ( $\varphi \approx 60^\circ$ ). The second type, being the dominant one, experiences electrostatic repulsion, causing the oxygen to move upward and slightly elevate above the position of the hydrogen atoms ( $\varphi \approx 140^\circ$ , Figure 4d). In either configuration, the OH bonds possess the ability to form hydrogen bonds with  $*CO$  and can act as proton donors for the  $*CO$  hydrogenation. For the  $K^+e^-$  environment, the approach of  $K^+$  at the interface exerts stronger disturbances to the interfacial region and diminishes the presence of adsorbed water with  $\varphi$  at  $\sim 60^\circ$ . A main peak at  $\sim 130^\circ$  in the  $\varphi$  distribution and two evident peaks at  $\sim 90^\circ$  and  $\sim 150^\circ$  in the  $\theta$  distribution are observed. This distribution clearly corresponds to the “one-H down” water configuration, where one OH bond is parallel to the interface and the other OH bond orients toward the interface. In the one-H down water, the hydrogen atom pointing toward the interface is challenging in forming hydrogen bonds with  $*CO$  and serving as the proton sources for  $*CO$  hydrogenation due to the required configuration flip. The other OH bond is prone to deviate from  $*CO$  due to the repulsion from  $K^+$  and thus is also difficult for the protonation of  $*CO$  (Figure 4d). Summarily, the interfacial water configuration under the  $Li^+$  condition will create a hydrogen-bond-rich environment, while that under  $K^+$  conditions will

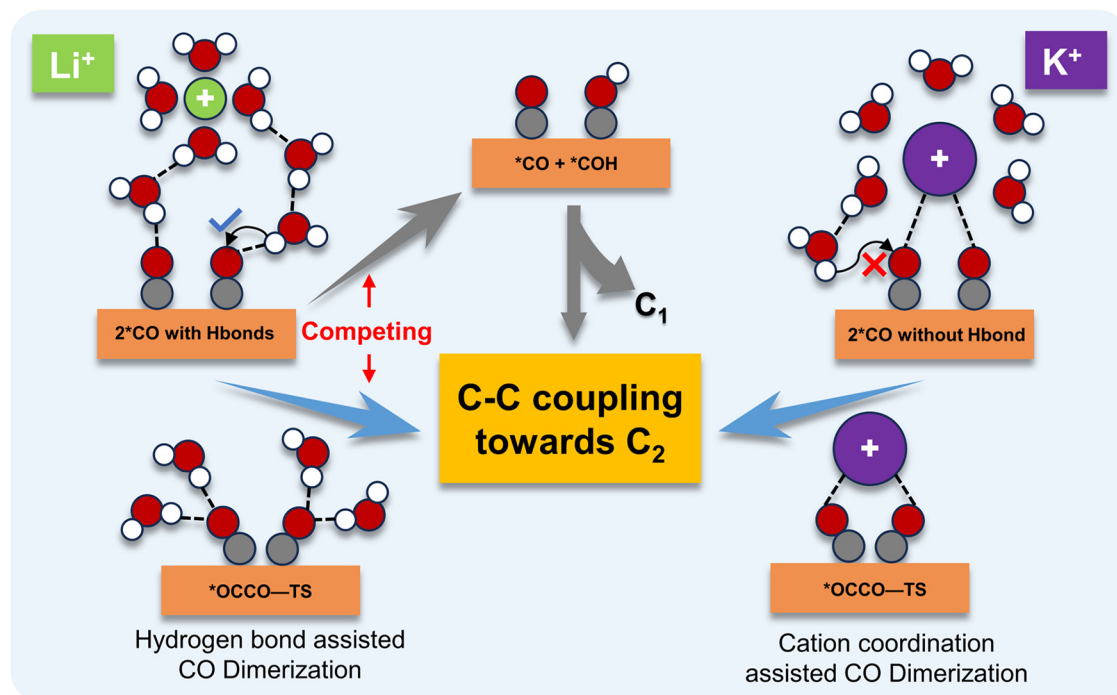


**Figure 5.** Schematic representation of the integrated mechanism elucidating the cation-dependent  $C_2$  selectivity through the combination effects of interfacial water molecules and cations.

result in weak hydrogen-bond interactions (Figure S20), which is consistent with recent experimental SEIRAS results carried out on Pt with different cations.<sup>74</sup>

Based on these qualitative understandings, the typical interfacial water molecules are selected for evaluating the kinetic barrier of  $*CO$  protonation to  $*COH$ . Under the condition of  $Li^+$ , most of the interfacial water molecules near  $*CO$  are located in the second solvation shell of  $Li^+$  without direct cation–water coordination interaction (Figure 4d and Figure S22). For  $K^+$ , there are interfacial water molecules that coordinate with  $K^+$  and those that do not coordinate with  $K^+$  in the vicinity of  $*CO$  due to its smaller solvation shell (Figure 4d and Figure S22). The calculation results show that the lowest activation energy is 1.10 eV in the  $K^+ + e^-$  model, while it is only 0.60 eV in the  $Li^+ + e^-$  model (Figure 4d), which is comparable to the activation energy of CO dimerization (0.56 eV). This implies that under a  $Li^+ + e^-$  environment, the protonation of  $*CO$  toward the  $C_1$  pathway is highly probable and will significantly compete with the course of C–C coupling. The relatively high activation energy in the  $K^+ + e^-$  model ensures that the adsorbed  $*CO$  is less likely to be hydrogenated while tending to undergo C–C coupling. To further corroborate this trend, we investigated the case of  $Cs^+ + e^-$ .  $Cs^+$  has a larger ionic radius and is more prone to approach the interface and also coordinate with the  $*CO + *CO$ . Results from free energy calculations of CO dimerization, radial distribution functions, the distribution of interfacial water configuration, and the activation energy calculations for  $*CO$  protonation (Figures S18, S19, and S21) demonstrate that  $Cs^+$  is actually more effective than  $K^+$  in preventing the protonation of  $*CO$  with fewer interfacial water molecules.

One may wonder whether the “one-H down” configuration of interfacial water in the  $M^+ + e^-$  model will benefit the HER due to the orientation of partial hydrogen toward the interface.

We calculate the activation energy for the Volmer step ( $H_2O + e^- \rightarrow *H + OH^-$ ) of the HER process. The results (Figure S24) reveal that the activation energies in  $M^+ + e^-$  ( $M = Li^+$ ,  $Na^+$ , and  $Cs^+$ ) environments are both about 1.1 eV. Our calculations do not reveal a discernible trend in the cation-dependent activation energy. Due to the larger hydrogen density associated with  $Li^+$  at the interface (Figure 4b), the  $Li^+ + e^-$  model is more likely to undergo the HER process from a probabilistic standpoint. A more detailed investigation that integrates experimental and theoretical approaches is necessary to decipher cation-dependent HER activity under the  $CO_2RR$  in the future. However, it can be observed that the activation energy of the Volmer step is greater than that of C–C coupling. Therefore, C–C coupling remains the favorable one in the competition with the HER. Additionally, the challenges associated with the Volmer step imply that the formation of surface-adsorbed hydrogen ( $*H$ ) is difficult. This further leads to another hydrogenation mode of  $*CO$  that is hard, which typically involves the reaction between  $*H$  and  $*CO$  to form  $*CHO$ .<sup>84</sup> Obtaining an H atom directly through interfacial water to form  $*CHO$  is even more energy prohibited (Figure S25).

Figure 5 describes the full picture of cation–water–adsorbate interactions to tune the selectivity of the  $C_2$  pathway. The smaller cation ( $Li^+$ ) tends to stay away from the interface, making it difficult to coordinate with  $*CO + *CO$ . This C–C coupling beyond the cation solvation shell is primarily stabilized by the hydrogen bonds provided by surrounding interfacial water molecules. However, besides stabilizing the coupling intermediates, the hydrogen bonds also tend to favor the formation of  $*COH$ . While the possibility of C–C coupling between  $*COH$  and  $*CO$  cannot be completely excluded, it is kinetically more difficult than CO dimerization. Simultaneously, the further protonation of  $*COH$  toward  $C_1$  products can be more readily anticipated

since the rate-limiting step of the  $C_1$  pathway has already been surmounted. Thus, the ability to generate  $C_2$  products is severely weakened. The larger cation ( $K^+$ ) manifests its modulation effect in its ability to coordinate with  $*CO+*CO$  within its solvation shell. Although this inner-sphere coordination negligibly contributes to the reaction barrier for C–C coupling, it reshapes the distribution around interfacial water, reducing the concentration of interfacial protons and creating a hydrophobic microenvironment with the absence of hydrogen bonds, thereby acting as a protective role for the initial state of the C–C coupling course. This prevents  $*CO$  from following the  $C_1$  pathway, serving as the primary factor of the cation-dependent increasing trend in  $C_2$  product selectivity.

Finally, we discuss the consistency with the experiments. Koper et al. demonstrated the  $C_2/C_1$  is higher with  $K^+$  than that of  $Li^+$ , around  $-0.6$  V vs RHE.<sup>34</sup> The above mechanism can directly offer a rationale for their observations. In our theory, the partially desolvated larger cation (e.g.,  $K^+$ ) can coordinate with the  $*CO+*CO$  to stabilize it and concurrently repulse the interfacial water to avoid  $*CO$  protonation and to enhance  $C_2$  selectivity. We can infer that if the interfacial water is further excluded through activity regulation, the  $C_2$  product will further increase, which has been confirmed by recent experiments.<sup>32</sup> However, if the cation cannot coordinate with the  $*CO+*CO$  but repulses the interfacial water, the C–C coupling will also be forbidden with high activation energy due to the lack of stabilization effect (Figure 1). The introduction of large alkylammonium cations, which cannot coordinate with the adsorbate due to its chain-like molecular structure but blocks the supply of interfacial water, suppresses the production of ethylene experimentally.<sup>85</sup> If the  $K^+$  cannot coordinate with the  $*CO+*CO$  and thus the water molecules can approach the intermediates (like the situation in  $Li^+$ ), the selectivity of  $C_2/C_1$  will also change according to our scenario. A recent experimental work anchored  $K^+$  into the cavity of the 18-crown-6 molecule, and thus the  $K^+$  cannot serve as a protector to directly coordinate with the  $*CO+*CO$ , which indeed facilitates the hydrogenation of  $*CO$ , resulting in a decrease in  $C_2$  products and an increase in  $C_1$  products.<sup>86</sup> It is noteworthy that this work was conducted under acidic conditions. Similar experimental results have also been reported under alkaline conditions, although with  $Na^+$ .<sup>87</sup> Combined with the calculation results that the location of  $Li^+$  and  $K^+$  cations and their interaction with adsorbates near the interface are similar under typical acidic and alkaline conditions with the neutral condition (Figure S26), we speculate that our mechanism may be applicable across a wide range of pH.

## CONCLUSION

To summarize, we have investigated the combined effect of interfacial water and alkali metal cations on the C–C coupling at the Cu(100) electrode/electrolyte interface using AIMD simulations with constrained MD and a slow-growth approach. We observe a linear correlation between the hydrogen bond stabilization effect of interfacial water on the carbon-containing intermediates and the corresponding alleviation in the C–C coupling free energy. Larger cations can coordinate with  $*OCCO$ , partially replacing the hydrogen bond stabilization of water. However, the energetic impact of different cations on the CO dimerization is minor, regardless of whether the cations coordinate with the  $*OCCO$  species. The primary

contributor to lower the energy barrier in C–C coupling is the charging of  $*CO$  induced by the electrode potential. Larger cations, upon coordination with  $*CO+*CO$ , can repel surrounding water molecules, creating a local hydrophobic environment with a scarcity of hydrogen bonds for the  $*CO+*CO$  configuration. This effectively mitigates the risk of  $*CO$  protonation toward the  $C_1$  pathway, representing the primary factor through which larger cations facilitate C–C coupling. Our work proposes a new mechanism for the understanding of the cation promoting effect by comprehensively considering the cation–water–adsorbate interactions at the atomic level. We anticipate that this study will provide useful insights of cations tuning the structure of the electric double layer for improving activity and selectivity of the  $CO_2RR$  toward multicarbon products.

## ASSOCIATED CONTENT

### Supporting Information

The Supporting Information is available free of charge at <https://pubs.acs.org/doi/10.1021/jacs.3c13602>.

Additional computational details; visualizations of the structural model; details of free energy calculations; additional information on  $*CO+*CHO$ ,  $*CO+*COH$ , and  $*CO+*C$  reactions; analysis of the cation's solvation behavior; more statistics on interfacial water; investigation of the  $Cs^+$  case; discussion on the pH effect (PDF)

## AUTHOR INFORMATION

### Corresponding Authors

Shisheng Zheng – School of Advanced Materials, Peking University, Shenzhen Graduate School, Shenzhen 518000, China; College of Energy, Xiamen University, Xiamen 361000, China; Email: [zhengss@pku.edu.cn](mailto:zhengss@pku.edu.cn)

Feng Pan – School of Advanced Materials, Peking University, Shenzhen Graduate School, Shenzhen 518000, China; [orcid.org/0000-0002-8216-1339](https://orcid.org/0000-0002-8216-1339); Email: [panfeng@pkusz.edu.cn](mailto:panfeng@pkusz.edu.cn)

### Authors

Xinzhe Yang – School of Advanced Materials, Peking University, Shenzhen Graduate School, Shenzhen 518000, China

Haowen Ding – School of Advanced Materials, Peking University, Shenzhen Graduate School, Shenzhen 518000, China

Shunning Li – School of Advanced Materials, Peking University, Shenzhen Graduate School, Shenzhen 518000, China; [orcid.org/0000-0002-5381-6025](https://orcid.org/0000-0002-5381-6025)

Jian-Feng Li – College of Energy, Xiamen University, Xiamen 361000, China; State Key Laboratory of Physical Chemistry of Solid Surfaces, iChEM, College of Chemistry and Chemical Engineering, College of Materials, College of Electronic Science and Engineering, College of Physical Science and Technology, Fujian Key Laboratory of Ultrafast Laser Technology and Applications, Xiamen University, Xiamen 361000, China; Innovation Laboratory for Sciences and Technologies of Energy Materials of Fujian Province (IKKEM), Xiamen 361000, China; [orcid.org/0000-0003-1598-6856](https://orcid.org/0000-0003-1598-6856)

Complete contact information is available at: <https://pubs.acs.org/10.1021/jacs.3c13602>

## Notes

The authors declare no competing financial interest.

## ACKNOWLEDGMENTS

The authors acknowledge financial support from the Guangdong Basic and Applied Basic Research Foundation (2020A1515110843), Chemistry and Chemical Engineering Guangdong Laboratory (Grant No. 1922018), National Natural Science Foundation of China (22109003), Natural Science Foundation of Shenzhen (JCYJ20190813110605381), and the Major Science and Technology Infrastructure Project of Material Genome Big-science Facilities Platform supported by Municipal Development and Reform Commission of Shenzhen.

## REFERENCES

- (1) Zhu, P.; Wang, H. High-purity and high-concentration liquid fuels through CO<sub>2</sub> electroreduction. *Nat. Catal.* **2021**, *4* (11), 943–951.
- (2) Schouten, K. J. P.; Calle-Vallejo, F.; Koper, M. T. A step closer to the electrochemical production of liquid fuels. *Angew. Chem., Int. Ed.* **2014**, *53* (41), 10858–10860.
- (3) Raciti, D.; Wang, C. Recent advances in CO<sub>2</sub> reduction electrocatalysis on copper. *ACS Energy Lett.* **2018**, *3* (7), 1545–1556.
- (4) Nitopi, S.; Bertheussen, E.; Scott, S. B.; Liu, X.; Engstfeld, A. K.; Horch, S.; Seger, B.; Stephens, I. E.; Chan, K.; Hahn, C. Progress and perspectives of electrochemical CO<sub>2</sub> reduction on copper in aqueous electrolyte. *Chem. Rev.* **2019**, *119* (12), 7610–7672.
- (5) Zhang, W.; Hu, Y.; Ma, L.; Zhu, G.; Wang, Y.; Xue, X.; Chen, R.; Yang, S.; Jin, Z. Progress and perspective of electrocatalytic CO<sub>2</sub> reduction for renewable carbonaceous fuels and chemicals. *Adv. Sci.* **2018**, *5* (1), 1700275.
- (6) Zhou, Y.; Che, F.; Liu, M.; Zou, C.; Liang, Z.; De Luna, P.; Yuan, H.; Li, J.; Wang, Z.; Xie, H. Dopant-induced electron localization drives CO<sub>2</sub> reduction to C<sub>2</sub> hydrocarbons. *Nat. Chem.* **2018**, *10* (9), 974–980.
- (7) Zhong, M.; Tran, K.; Min, Y.; Wang, C.; Wang, Z.; Dinh, C.-T.; De Luna, P.; Yu, Z.; Rasouli, A. S.; Brodersen, P.; et al. Accelerated discovery of CO<sub>2</sub> electrocatalysts using active machine learning. *Nature* **2020**, *581* (7807), 178–183.
- (8) Zhuang, T.-T.; Liang, Z.-Q.; Seifitokaldani, A.; Li, Y.; De Luna, P.; Burdyny, T.; Che, F.; Meng, F.; Min, Y.; Quintero-Bermudez, R.; et al. Steering post-C-C coupling selectivity enables high efficiency electroreduction of carbon dioxide to multi-carbon alcohols. *Nat. Catal.* **2018**, *1* (6), 421–428.
- (9) Zhuang, T.-T.; Pang, Y.; Liang, Z.-Q.; Wang, Z.; Li, Y.; Tan, C.-S.; Li, J.; Dinh, C. T.; De Luna, P.; Hsieh, P.-L.; et al. Copper nanocavities confine intermediates for efficient electrosynthesis of C<sub>3</sub> alcohol fuels from carbon monoxide. *Nat. Catal.* **2018**, *1* (12), 946–951.
- (10) Xu, H.; Rebolgar, D.; He, H.; Chong, L.; Liu, Y.; Liu, C.; Sun, C.-J.; Li, T.; Muntean, J. V.; Winans, R. E.; et al. Highly selective electrocatalytic CO<sub>2</sub> reduction to ethanol by metallic clusters dynamically formed from atomically dispersed copper. *Nat. Energy* **2020**, *5* (8), 623–632.
- (11) Liang, Z.-Q.; Zhuang, T.-T.; Seifitokaldani, A.; Li, J.; Huang, C.-W.; Tan, C.-S.; Li, Y.; De Luna, P.; Dinh, C. T.; Hu, Y.; et al. Copper-on-nitride enhances the stable electrosynthesis of multicarbon products from CO<sub>2</sub>. *Nat. Commun.* **2018**, *9* (1), 3828.
- (12) Ma, Z.; Yang, Z.; Lai, W.; Wang, Q.; Qiao, Y.; Tao, H.; Lian, C.; Liu, M.; Ma, C.; Pan, A.; et al. CO<sub>2</sub> electroreduction to multicarbon products in strongly acidic electrolyte via synergistically modulating the local microenvironment. *Nat. Commun.* **2022**, *13* (1), 7596.
- (13) Liu, M.; Pang, Y.; Zhang, B.; De Luna, P.; Voznyy, O.; Xu, J.; Zheng, X.; Dinh, C. T.; Fan, F.; Cao, C.; et al. Enhanced electrocatalytic CO<sub>2</sub> reduction via field-induced reagent concentration. *Nature* **2016**, *537* (7620), 382–386.
- (14) Wang, X.; Wang, Z.; García de Arquer, F. P.; Dinh, C.-T.; Ozden, A.; Li, Y. C.; Nam, D.-H.; Li, J.; Liu, Y.-S.; Wicks, J.; et al. Efficient electrically powered CO<sub>2</sub>-to-ethanol via suppression of deoxygenation. *Nat. Energy* **2020**, *5* (6), 478–486.
- (15) Deng, B.; Huang, M.; Zhao, X.; Mou, S.; Dong, F. Interfacial electrolyte effects on electrocatalytic CO<sub>2</sub> reduction. *ACS Catal.* **2022**, *12* (1), 331–362.
- (16) García de Arquer, F. P.; Dinh, C.-T.; Ozden, A.; Wicks, J.; McCallum, C.; Kirmani, A. R.; Nam, D.-H.; Gabardo, C.; Seifitokaldani, A.; Wang, X.; et al. CO<sub>2</sub> electrolysis to multicarbon products at activities greater than 1 A cm<sup>-2</sup>. *Science* **2020**, *367* (6478), 661–666.
- (17) Garg, S.; Li, M.; Rufford, T. E.; Ge, L.; Rudolph, V.; Knibbe, R.; Konarova, M.; Wang, G. G. Catalyst-electrolyte interactions in aqueous reline solutions for highly selective electrochemical CO<sub>2</sub> reduction. *ChemSusChem* **2020**, *13* (2), 304–311.
- (18) Thorson, M. R.; Siil, K. I.; Kenis, P. J. Effect of cations on the electrochemical conversion of CO<sub>2</sub> to CO. *J. Electrochem. Soc.* **2013**, *160* (1), F69.
- (19) Li, C.-Y.; Le, J.-B.; Wang, Y.-H.; Chen, S.; Yang, Z.-L.; Li, J.-F.; Cheng, J.; Tian, Z.-Q. In situ probing electrified interfacial water structures at atomically flat surfaces. *Nat. Mater.* **2019**, *18* (7), 697–701.
- (20) Carrasco, J.; Hodgson, A.; Michaelides, A. A molecular perspective of water at metal interfaces. *Nat. Mater.* **2012**, *11* (8), 667–674.
- (21) Wang, Y.-H.; Zheng, S.; Yang, W.-M.; Zhou, R.-Y.; He, Q.-F.; Radjenovic, P.; Dong, J.-C.; Li, S.; Zheng, J.; Yang, Z.-L.; et al. In situ Raman spectroscopy reveals the structure and dissociation of interfacial water. *Nature* **2021**, *600* (7887), 81–85.
- (22) Björneholm, O.; Hansen, M. H.; Hodgson, A.; Liu, L.-M.; Limmer, D. T.; Michaelides, A.; Pedevilla, P.; Rossmeisl, J.; Shen, H.; Tocci, G.; et al. Water at interfaces. *Chem. Rev.* **2016**, *116* (13), 7698–7726.
- (23) Groß, A.; Sakong, S. Ab initio simulations of water/metal interfaces. *Chem. Rev.* **2022**, *122* (12), 10746–10776.
- (24) Xu, Y.; Ma, Y.-B.; Gu, F.; Yang, S.-S.; Tian, C.-S. Structure evolution at the gate-tunable suspended graphene-water interface. *Nature* **2023**, *621* (7979), 506–510.
- (25) Zheng, S.; Liang, X.; Pan, J.; Hu, K.; Li, S.; Pan, F. Multi-Center Cooperativity Enables Facile C-C Coupling in Electrochemical CO<sub>2</sub> Reduction on a Ni<sub>2</sub>P Catalyst. *ACS Catal.* **2023**, *13* (5), 2847–2856.
- (26) Santatiwongchai, J.; Faungnawakij, K.; Hirunsit, P. Comprehensive mechanism of CO<sub>2</sub> electroreduction toward ethylene and ethanol: the solvent effect from explicit water-Cu (100) interface models. *ACS Catal.* **2021**, *11* (15), 9688–9701.
- (27) Heenen, H. H.; Gauthier, J. A.; Kristoffersen, H. H.; Ludwig, T.; Chan, K. Solvation at metal/water interfaces: An ab initio molecular dynamics benchmark of common computational approaches. *J. Chem. Phys.* **2020**, *152* (14), .
- (28) Ludwig, T.; Gauthier, J. A.; Brown, K. S.; Ringe, S.; Nørskov, J. K.; Chan, K. Solvent-adsorbate interactions and adsorbate-specific solvent structure in carbon dioxide reduction on a stepped Cu surface. *J. Phys. Chem. C* **2019**, *123* (10), 5999–6009.
- (29) Wu, J.; Huang, Y.; Ye, W.; Li, Y. CO<sub>2</sub> reduction: from the electrochemical to photochemical approach. *Adv. Sci.* **2017**, *4* (11), 1700194.
- (30) Vasileff, A.; Xu, C.; Jiao, Y.; Zheng, Y.; Qiao, S.-Z. Surface and interface engineering in copper-based bimetallic materials for selective CO<sub>2</sub> electroreduction. *Chem.* **2018**, *4* (8), 1809–1831.
- (31) Liu, T.; Wang, Y.; Li, Y. Can Metal-Nitrogen-Carbon Single-Atom Catalysts Boost the Electroreduction of Carbon Monoxide? *JACS Au* **2023**, *3* (3), 943–952.
- (32) Zhang, H.; Gao, J.; Raciti, D.; Hall, A. S. Promoting Cu-catalysed CO<sub>2</sub> electroreduction to multicarbon products by tuning the activity of H<sub>2</sub>O. *Nat. Catal.* **2023**, 1–11.

- (33) Resasco, J.; Chen, L. D.; Clark, E.; Tsai, C.; Hahn, C.; Jaramillo, T. F.; Chan, K.; Bell, A. T. Promoter effects of alkali metal cations on the electrochemical reduction of carbon dioxide. *J. Am. Chem. Soc.* **2017**, *139* (32), 11277–11287.
- (34) Pérez-Gallent, E.; Marcandalli, G.; Figueiredo, M. C.; Calle-Vallejo, F.; Koper, M. T. Structure-and potential-dependent cation effects on CO reduction at copper single-crystal electrodes. *J. Am. Chem. Soc.* **2017**, *139* (45), 16412–16419.
- (35) Singh, M. R.; Kwon, Y.; Lum, Y.; Ager, J. W., III; Bell, A. T. Hydrolysis of electrolyte cations enhances the electrochemical reduction of CO<sub>2</sub> over Ag and Cu. *J. Am. Chem. Soc.* **2016**, *138* (39), 13006–13012.
- (36) Ringe, S.; Clark, E. L.; Resasco, J.; Walton, A.; Seger, B.; Bell, A. T.; Chan, K. Understanding cation effects in electrochemical CO<sub>2</sub> reduction. *Energy Environ. Sci.* **2019**, *12* (10), 3001–3014.
- (37) Ovalle, V. J.; Hsu, Y.-S.; Agrawal, N.; Janik, M. J.; Waagele, M. M. Correlating hydration free energy and specific adsorption of alkali metal cations during CO<sub>2</sub> electroreduction on Au. *Nat. Catal.* **2022**, *5* (7), 624–632.
- (38) Liu, H.; Liu, J.; Yang, B. Promotional role of a cation intermediate complex in C<sub>2</sub> formation from electrochemical reduction of CO<sub>2</sub> over Cu. *ACS Catal.* **2021**, *11* (19), 12336–12343.
- (39) Bagger, A.; Arnarson, L.; Hansen, M. H.; Spohr, E.; Rossmeisl, J. Electrochemical CO reduction: A property of the electrochemical interface. *J. Am. Chem. Soc.* **2019**, *141* (4), 1506–1514.
- (40) Wang, Y.-H.; Li, S.; Zhou, R.-Y.; Zheng, S.; Zhang, Y.-J.; Dong, J.-C.; Yang, Z.-L.; Pan, F.; Tian, Z.-Q.; Li, J.-F. In situ electrochemical Raman spectroscopy and ab initio molecular dynamics study of interfacial water on a single-crystal surface. *Nat. Protoc.* **2023**, *18* (3), 883–901.
- (41) Le, J.-B.; Chen, A.; Kuang, Y.; Cheng, J. Molecular understanding of cation effects on double layer and its significance to CO-CO dimerization. *Natl. Sci. Rev.* **2023**, *10*, nwad105.
- (42) Monteiro, M. C.; Dattila, F.; Hagedoorn, B.; García-Muelas, R.; López, N.; Koper, M. T. Absence of CO<sub>2</sub> electroreduction on copper, gold and silver electrodes without metal cations in solution. *Nat. Catal.* **2021**, *4* (8), 654–662.
- (43) Qin, X.; Hansen, H. A.; Honkala, K.; Melander, M. M. Cation-induced changes in the inner-and outer-sphere mechanisms of electrocatalytic CO<sub>2</sub> reduction. *Nat. Commun.* **2023**, *14* (1), 7607.
- (44) Kim, Y.-G.; Baricuatro, J. H.; Javier, A.; Gregoire, J. M.; Soriaga, M. P. The evolution of the polycrystalline copper surface, first to Cu (111) and then to Cu (100), at a fixed CO<sub>2</sub>RR potential: a study by operando EC-STM. *Langmuir* **2014**, *30* (50), 15053–15056.
- (45) Schouten, K. J. P.; Pérez Gallent, E.; Koper, M. T. Structure sensitivity of the electrochemical reduction of carbon monoxide on copper single crystals. *ACS Catal.* **2013**, *3* (6), 1292–1295.
- (46) Kresse, G.; Hafner, J. Ab initio molecular dynamics for liquid metals. *Phys. Rev. B* **1993**, *47* (1), 558.
- (47) Kresse, G.; Furthmüller, J. Efficient iterative schemes for ab initio total-energy calculations using a plane-wave basis set. *Phys. Rev. B* **1996**, *54* (16), 11169.
- (48) Blöchl, P. E. Projector augmented-wave method. *Phys. Rev. B* **1994**, *50* (24), 17953.
- (49) Perdew, J. P.; Burke, K.; Ernzerhof, M. Generalized gradient approximation made simple. *Phys. Rev. Lett.* **1996**, *77* (18), 3865.
- (50) Grimme, S.; Antony, J.; Ehrlich, S.; Krieg, H. A consistent and accurate ab initio parametrization of density functional dispersion correction (DFT-D) for the 94 elements H-Pu. *J. Chem. Phys.* **2010**, *132* (15), .
- (51) Henkelman, G.; Uberuaga, B. P.; Jónsson, H. A climbing image nudged elastic band method for finding saddle points and minimum energy paths. *J. Chem. Phys.* **2000**, *113* (22), 9901–9904.
- (52) Henkelman, G.; Jónsson, H. A dimer method for finding saddle points on high dimensional potential surfaces using only first derivatives. *J. Chem. Phys.* **1999**, *111* (15), 7010–7022.
- (53) Woo, T. K.; Margl, P. M.; Blöchl, P. E.; Ziegler, T. A Combined Car-Parrinello QM/MM Implementation for ab Initio Molecular Dynamics Simulations of Extended Systems: Application to Transition Metal Catalysis. *J. Phys. Chem. B* **1997**, *101* (40), 7877–7880.
- (54) Jarzynski, C. Nonequilibrium equality for free energy differences. *Phys. Rev. Lett.* **1997**, *78* (14), 2690.
- (55) Bodenschatz, C. J.; Sarupria, S.; Getman, R. B. Molecular-level details about liquid H<sub>2</sub>O interactions with CO and sugar alcohol adsorbates on Pt (111) calculated using density functional theory and molecular dynamics. *J. Phys. Chem. C* **2015**, *119* (24), 13642–13651.
- (56) Yu, S.; Levell, Z.; Jiang, Z.; Zhao, X.; Liu, Y. What Is the Rate-Limiting Step of Oxygen Reduction Reaction on Fe-N-C Catalysts? *J. Am. Chem. Soc.* **2023**, *145* (46), 25352–25356.
- (57) Qian, S.-J.; Cao, H.; Chen, J.-W.; Chen, J.-C.; Wang, Y.-G.; Li, J. Critical role of explicit inclusion of solvent and electrode potential in the electrochemical description of nitrogen reduction. *ACS Catal.* **2022**, *12* (18), 11530–11540.
- (58) Kristoffersen, H. H.; Chan, K. Towards constant potential modeling of CO-CO coupling at liquid water-Cu (100) interfaces. *J. Catal.* **2021**, *396*, 251–260.
- (59) Zhao, Y.; Zhang, X.-G.; Bodappa, N.; Yang, W.-M.; Liang, Q.; Radjenovica, P. M.; Wang, Y.-H.; Zhang, Y.-J.; Dong, J.-C.; Tian, Z.-Q. Elucidating electrochemical CO<sub>2</sub> reduction reaction processes on Cu (hkl) single-crystal surfaces by in situ Raman spectroscopy. *Energy Environ. Sci.* **2022**, *15* (9), 3968–3977.
- (60) Kim, Y.; Park, S.; Shin, S.-J.; Choi, W.; Min, B. K.; Kim, H.; Kim, W.; Hwang, Y. J. Time-resolved observation of C-C coupling intermediates on Cu electrodes for selective electrochemical CO<sub>2</sub> reduction. *Energy Environ. Sci.* **2020**, *13* (11), 4301–4311.
- (61) Montoya, J. H.; Shi, C.; Chan, K.; Nørskov, J. K. Theoretical insights into a CO dimerization mechanism in CO<sub>2</sub> electroreduction. *J. Phys. Chem. Lett.* **2015**, *6* (11), 2032–2037.
- (62) Liu, X.; Schlexer, P.; Xiao, J.; Ji, Y.; Wang, L.; Sandberg, R. B.; Tang, M.; Brown, K. S.; Peng, H.; Ringe, S.; et al. pH effects on the electrochemical reduction of CO<sub>2</sub> towards C<sub>2</sub> products on stepped copper. *Nat. Commun.* **2019**, *10* (1), 32.
- (63) Xiao, H.; Cheng, T.; Goddard, W. A., III; Sundararaman, R. Mechanistic explanation of the pH dependence and onset potentials for hydrocarbon products from electrochemical reduction of CO on Cu (111). *J. Am. Chem. Soc.* **2016**, *138* (2), 483–486.
- (64) Peng, H.; Tang, M. T.; Liu, X.; Lamoureux, P. S.; Bajdich, M.; Abild-Pedersen, F. The role of atomic carbon in directing electrochemical CO<sub>2</sub> reduction to multicarbon products. *Energy Environ. Sci.* **2021**, *14* (1), 473–482.
- (65) Gauthier, J. A.; Lin, Z.; Head-Gordon, M.; Bell, A. T. Pathways for the Formation of C<sub>2</sub><sup>+</sup> Products under Alkaline Conditions during the Electrochemical Reduction of CO<sub>2</sub>. *ACS Energy Lett.* **2022**, *7* (5), 1679–1686.
- (66) Cheng, T.; Xiao, H.; Goddard, W. A., III Full atomistic reaction mechanism with kinetics for CO reduction on Cu (100) from ab initio molecular dynamics free-energy calculations at 298 K. *Proc. Natl. Acad. Sci. U.S.A.* **2017**, *114* (8), 1795–1800.
- (67) Xiao, H.; Goddard, W. A., III; Cheng, T.; Liu, Y. Cu metal embedded in oxidized matrix catalyst to promote CO<sub>2</sub> activation and CO dimerization for electrochemical reduction of CO<sub>2</sub>. *Proc. Natl. Acad. Sci. U.S.A.* **2017**, *114* (26), 6685–6688.
- (68) Cheng, T.; Fortunelli, A.; Goddard, W. A., III Reaction intermediates during operando electrocatalysis identified from full solvent quantum mechanics molecular dynamics. *Proc. Natl. Acad. Sci. U.S.A.* **2019**, *116* (16), 7718–7722.
- (69) Wang, X.; Ou, P.; Ozden, A.; Hung, S.-F.; Tam, J.; Gabardo, C. M.; Howe, J. Y.; Sisler, J.; Bertens, K.; García de Arquer, F. P.; et al. Efficient electrosynthesis of n-propanol from carbon monoxide using a Ag-Ru-Cu catalyst. *Nat. Energy* **2022**, *7* (2), 170–176.
- (70) Wang, X.; Wang, Z.; Zhuang, T.-T.; Dinh, C.-T.; Li, J.; Nam, D.-H.; Li, F.; Huang, C.-W.; Tan, C.-S.; Chen, Z.; et al. Efficient upgrading of CO to C<sub>3</sub> fuel using asymmetric C-C coupling active sites. *Nat. Commun.* **2019**, *10* (1), 5186.
- (71) Li, J.; Zhang, Y.; Kuruvinashetti, K.; Kornienko, N. Construction of C-N bonds from small-molecule precursors through heterogeneous electrocatalysis. *Nat. Rev. Chem.* **2022**, *6* (5), 303–319.

- (72) Kim, J. E.; Choi, S.; Balamurugan, M.; Jang, J. H.; Nam, K. T. Electrochemical C-N bond formation for sustainable amine synthesis. *Trends Chem.* **2020**, *2* (11), 1004–1019.
- (73) Lv, C.; Zhong, L.; Liu, H.; Fang, Z.; Yan, C.; Chen, M.; Kong, Y.; Lee, C.; Liu, D.; Li, S.; et al. Selective electrocatalytic synthesis of urea with nitrate and carbon dioxide. *Nat. Sustain.* **2021**, *4* (10), 868–876.
- (74) Huang, B.; Rao, R. R.; You, S.; Hpone Myint, K.; Song, Y.; Wang, Y.; Ding, W.; Giordano, L.; Zhang, Y.; Wang, T.; et al. Cation- and pH-dependent hydrogen evolution and oxidation reaction kinetics. *JACS Au* **2021**, *1* (10), 1674–1687.
- (75) Rebstock, J. A.; Zhu, Q.; Baker, L. R. Comparing interfacial cation hydration at catalytic active sites and spectator sites on gold electrodes: understanding structure sensitive CO<sub>2</sub> reduction kinetics. *Chem. Sci.* **2022**, *13* (25), 7634–7643.
- (76) Schouten, K. J. P.; Qin, Z.; Pérez Gallent, E.; Koper, M. T. Two pathways for the formation of ethylene in CO reduction on single-crystal copper electrodes. *J. Am. Chem. Soc.* **2012**, *134* (24), 9864–9867.
- (77) Xiang, S.-Q.; Shi, J.-L.; Gao, S.-T.; Zhang, W.; Zhao, L.-B. Thermodynamic and kinetic competition between C-H and O-H bond formation pathways during electrochemical reduction of CO on copper electrodes. *ACS Catal.* **2021**, *11* (4), 2422–2434.
- (78) Shao, F.; Xia, Z.; You, F.; Wong, J. K.; Low, Q. H.; Xiao, H.; Yeo, B. S. Surface water as an initial proton source for the electrochemical CO reduction reaction on copper surfaces. *Angew. Chem., Int. Ed.* **2023**, *62* (3), No. e202214210.
- (79) Nie, X.; Esopi, M. R.; Janik, M. J.; Asthagiri, A. Selectivity of CO<sub>2</sub> reduction on copper electrodes: the role of the kinetics of elementary steps. *Angew. Chem., Int. Ed.* **2013**, *52* (9), 2459–2462.
- (80) Zhao, Q.; Martinez, J. M. P.; Carter, E. A. Electrochemical Hydrogenation of CO on Cu (100): Insights from Accurate Multiconfigurational Wavefunction Methods. *J. Phys. Chem. Lett.* **2022**, *13* (44), 10282–10290.
- (81) Yan, H.-M.; Wang, Z.-X.; Wang, Y.-M.; Xia, G.-J.; Wang, Y.-G. Fast Transformation of CO<sub>2</sub> into CO Via a Hydrogen Bond Network on the Cu Electrocatalysts. *J. Phys. Chem. C* **2022**, *126* (18), 7841–7848.
- (82) Li, X. Y.; Wang, T.; Cai, Y. C.; Meng, Z. D.; Nan, J. W.; Ye, J. Y.; Yi, J.; Zhan, D. P.; Tian, N.; Zhou, Z. Y. Mechanism of Cations Suppressing Proton Diffusion Kinetics for Electrocatalysis. *Angew. Chem., Int. Ed.* **2023**, *62* (14), No. e202218669.
- (83) Li, P.; Jiao, Y.; Ruan, Y.; Fei, H.; Men, Y.; Guo, C.; Wu, Y.; Chen, S. Revealing the role of double-layer microenvironments in pH-dependent oxygen reduction activity over metal-nitrogen-carbon catalysts. *Nat. Commun.* **2023**, *14* (1), 6936.
- (84) Cheng, T.; Xiao, H.; Goddard, W. A., III Free-energy barriers and reaction mechanisms for the electrochemical reduction of CO on the Cu (100) surface, including multiple layers of explicit solvent at pH 0. *J. Phys. Chem. Lett.* **2015**, *6* (23), 4767–4773.
- (85) Li, J.; Li, X.; Gunathunge, C. M.; Waagele, M. M. Hydrogen bonding steers the product selectivity of electrocatalytic CO reduction. *Proc. Natl. Acad. Sci. U.S.A.* **2019**, *116* (19), 9220–9229.
- (86) Xu, K.; Li, J.; Liu, F.; Chen, X.; Zhao, T.; Cheng, F. Favoring CO Intermediate Stabilization and Protonation by Crown Ether for CO<sub>2</sub> Electromethanation in Acidic Media. *Angew. Chem., Int. Ed.* **2023**, *62* (50), No. e202311968.
- (87) Li, J.; Wu, D.; Malkani, A. S.; Chang, X.; Cheng, M.-J.; Xu, B.; Lu, Q. Hydroxide Is Not a Promoter of C<sub>2</sub><sup>+</sup> Product Formation in the Electrochemical Reduction of CO on Copper. *Angew. Chem., Int. Ed.* **2020**, *59* (11), 4464–4469.